Linear, nonlinear optical susceptibilities, hyperpolarizability, and space electronic charge density of meso silver(I) histidinate [Ag(D-his)]$_n$ (Hhis = histidine)

Saleem Ayaz Khan [a], A.H. Reshak [a,b,*]

[a] New Technologies – Research Center, University of West Bohemia, Univerzitni 8, 306 14 Pilsen, Czech Republic
[b] Center of Excellence Geopolymer and Green Technology, School of Material Engineering, University Malaysia Perlis, 01007 Kangar, Perlis, Malaysia

ARTICLE INFO

ABSTRACT

Full potential linear augmented plane wave method was used to calculate the electronic band structure, density of states, charge density and optical properties of meso silver(I) histidinate [Ag(D-his)]$_n$. The band structure investigation elucidated that the investigated compound possess indirect ($Z \rightarrow \Gamma$) broad gap. The effective mass ratio for electron, light hole and heavy hole were calculated in conduction band minimum (0.0596), upper valence band maximum (0.5085) and lower valence band maximum (0.3612) respectively. The total valence charge density shows covalent nature of [Ag(D-his)]$_n$ bonds. The compound contains two heterodimers per unit cell. The calculated length of the O–H bond that formed heterodimer is 1.67 Å. The average value of real and imaginary part of dielectric function were calculated. The three principal tensor components of $\varepsilon_2(\omega)$, $\varepsilon_1(\omega)$, $n(\omega)$, $I(\omega)$ and $R(\omega)$ were calculated and discussed in detail. The calculated uniaxial anisotropic value (0.0985) and birefringence (0.06) has indicated the strong anisotropy of the dielectric function in [Ag(D-his)]$_n$. The investigation of $n(\omega)$ spectra shows the superluminality in ultraviolet region while $R(\omega)$ spectra shows that [Ag(D-his)]$_n$ is suitable for antireflection coating material for solar cells in infrared and visible region. The investigated compound also exhibit second harmonic generation of about 1.57 pm/V at static limit and 2.34 pm/V at λ = 1064 nm. We have also calculated the microscopic first hyperpolarizability $\beta_{213}(\omega)$ for the dominant component $\chi^{(2)}_{213}(\omega)$ at static limit 0.666×10^{-30} esu and at λ = 1064 nm (0.965×10^{-30} esu).

© 2014 Published by Elsevier Ltd.

1. Introduction

The importance of metal complexes in biological systems cannot be ignored due to wide scope for the interaction of metal ions and biological molecules. Iron porphyrin complex in hemoglobin is responsible for oxygen storage and transport in the body tissues [1]. Metal ion like zinc perform important role in order to regulate the function of genes in the nuclei of cells. It is natural constituent of insulin, essential to the regulation of sugar metabolism [2]. Similarly calcium is the basis of bones and teeth. It is plentiful metal by mass in animals and human body [3]. Other examples are metals like iron, zinc, copper and manganese are included into catalytic proteins which facilitate a multitude of chemical reactions needed

for life. Various types of drug containing metals are used as a diagnostic agent for treatment of a variety of diseases [3–6].

Among them, silver complexes are the most important metal compounds used as antimicrobial agents in medicine. Silver is low toxic and active at low concentration [7,8]. Significant work has been done on silver(I) protein and silver(I) peptide interactions and silver(I) complexes with amino acids [9–15]. The crystal structures of many silver(I) complexes with amino-acids have been reported. {[Ag(Hglygly)]NO$_3$}$_2$, [Ag(gly)]$_n$ [9], [Ag(gly)]$_2$·H$_2$O}$_n$, [Ag(D- or L-asn)]$_n$, [Ag$_2$(D-asp)(L-asp)·1·5H$_2$O]$_n$ [10], [Ag(α-ala)]$_n$ [11] and [Ag(L-his)]$_n$ (L-3) [12], {[Ag(b-ala)]NO$_3$}$_2$ [13,14], (Hgly-gly = glycylglycine, Hala = alanine, Hgly = glycine, H$_2$asp = aspartic acid, Hasn = sparagines, and Hhis = histidine). The ligand-exchangeability is very important and play main role for antimicrobial activities of silver(I) complexes [15–17]. The silver(I) histidinate complexes are unique among silver(I) complexes with amino-acid ligands. Kasuga et al. [18] prepared D-isomer and meso silver(I) complexes in order to investigate ligand exchangeability and effect of chirality on structure of silver(I) histidinate and synthesized the

coordination polymer D-3 and meso silver(I) histidinate and its structural characterization. They reported that messo silver histadinate $[Ag(D\text{-}his)]_n$ is water-insoluble right-handed helical complex form by the reaction of Ag_2O and D-Hhis (Hhis = histidine). It is a good antimicrobial agent against some preferred bacteria (*Bacillus subtilis*, *Staphylococcus aureus*, *Pseudomonas aeruginosa* and *Escherichia coli*), molds (*Penicillium citrinum* and *Aspergillus niger*) yeasts (*Saccharomyces cerevisiae* and *Candida albicans*).

To the best of our knowledge no comprehensive DFT work is done for calculating the specific features of $[Ag(D\text{-}his)]_n$. In the present work we have addressed ourselves to calculate the structural, electronic, and optical properties of this important compound using the all-electron full potential linear augmented plane wave (FP-LAPW) method which has proven to be one of the most accurate methods [19–23] for the computation of the electronic structure of solids within a framework density functional theory (DFT).

2. Crystal structure and method of calculation

Meso silver histidinate $[Ag(D\text{-}his)]_n$ has the chemical formula $C_6H_8O_2N_3Ag$. It is stable in monoclinic phase having space group $P2_1$ (No. 4) that contain two formulas per unit cell. The lattice parameters are $a = 5.730$ Å, $b = 7.586$ Å, $c = 9.041$ Å with $\beta = 104.785°$. The crystallographic data of $[Ag(D\text{-}his)]_n$ have been taken from Cambridge Crystallographic data Center [24]. The deposition number is 789714 for supplementary crystallographic data

Fig. 1. (a) Molecular structure; (b) unit cell of $[Ag(D\text{-}his)]_n$ semiconductor.

(CCDC). Fig. 1 shows the molecular structure and unit cell of $[Ag(D\text{-}his)]_n$.

We have used the full potential linear augmented plane wave (FPLAPW) method within the framework of WIEN2k code [25], to calculate the electronic band structure, density of state, electronic charge density and optical properties of $[Ag(D\text{-}his)]_n$. Four schemes namely Ceperley–Alder (CA) local density approximation (CA-LDA) approach [26], Perdew–Burke–Ernzerhof generalized gradient approximation (PBE-GGA) [27], and Engel Voskov generalized gradient approximation (EV-GGA) [28] and the most recent modified Becke and Johnson (mBJ) approximation [29] were used for solve the exchange correlation potential. In order to converge the energy eigenvalues the wave function in the interstitial regions were expended in plane waves with cutoff $R_{MT}K_{max} = 7.0$. Where R_{MT} represent the muffin-tin (MT) sphere radius and K_{max} represent the magnitude of largest K vector in plane wave expansion. The selected muffin-tin (MT) sphere radii (R_{MT}) are 1.10 a.u. for C atom, 0.55 a.u. for H, 1.98 a.u. for Ag, 1.02 a.u for N and 1.12 a.u. for O atom. The wave function inside the sphere was expended up to $l_{max} = 10$ whereas the Fourier expansion of the charge density was up to $G_{max} = 26\ (a.u.)^{-1}$. We have optimized the structure by minimization of forces acting on the atoms. The convergence of the self-consistent calculations were done by the difference in total energy of the crystal did not exceed 10^{-5} Ryd for successive steps. The self consistencies were obtained by 120 **k** points in irreducible Brillion zones (IBZ), initiated from 500 **k** points in the Brillion zones (BZ).

3. Result and discussion

3.1. Band structure and density of state

The band structure and total density of state of $[Ag(D\text{-}his)]_n$ were calculated by CA-LDA, PBE-GGA, EV-GGA and mBJ as shown in Fig. 2a and b. The calculated band gap (E_g) values are shown in Table 1. The mBJ potential was selected for better band splitting and according to our previous experience that mBJ potential give an energy gap close to the experimental one [30–36] therefore it was selected for further investigation of partial density of states. The calculated band structure disclose that $[Ag(D\text{-}his)]_n$ possess indirect band gap ($Z \rightarrow \Gamma$). The effective mass of light hole (m_{lh}^*), heavy hole (m_{hh}^*) and electron (m_e^*) were calculated by fitting the valence and conduction bands extrema to the parabola according to the expression $E = \frac{\hbar^2 k^2}{2 m_e m^*}$ where m_e stands for rest mass of electron. The effective mass ratio of light hole (m_{lh}^*/m_e), heavy hole (m_{hh}^*/m_e) and electron (m_e^*/m_e) were calculated in lower valence band maximum (0.3612), upper valence band maximum (0.5085) and conduction band minimum (0.0596), respectively.

Fig. 3a–d illustrates the partial density of states (PDOS) which elucidate that the core bands around −12.5 eV are primarily formed by strongly hybridized C-2p and O-2s states with negligible role of H-1s and C-2s states. Around −12.0 eV both C-2s and N-2s states show strong hybridization which results in strong covalent bond between N and C atoms. In the energy range between −10.0 and −5.0 eV the bands are originated from strongly hybridized H-1s and O-2s, C-2p and dominant Ag-4d state. The valence bands between (−2.5 to −1.0 eV) are mainly constructed by Ag-4d state with negligible contribution of Ag-5s/2p and C-2p states. The upper valence band is mainly composed of predominant Ag-4d state with small contribution of Ag-5s state. The conduction band is formed by the contribution of C-2p and Ag-2p/4d states. Around 7.0 eV the bands formation occur by combination of Ag-5s/2p, C-2p and O-2s states. Ag-2p and O-2s show weak hybridization in this energy range. For higher energy range (7.4–17.5 eV) Ag-2p state is foremost while the contribution of C-2s/2p, N-2s
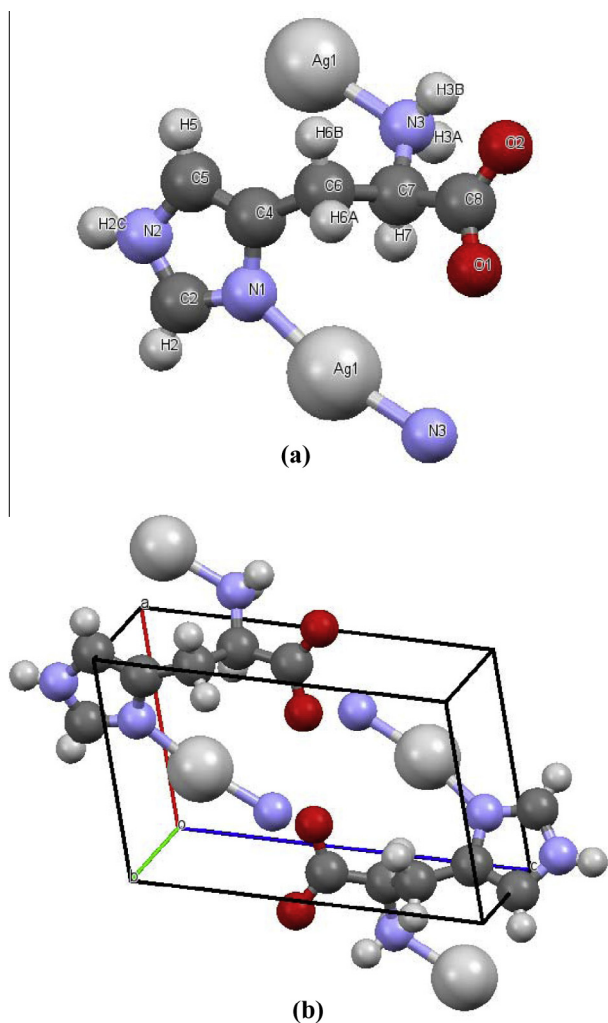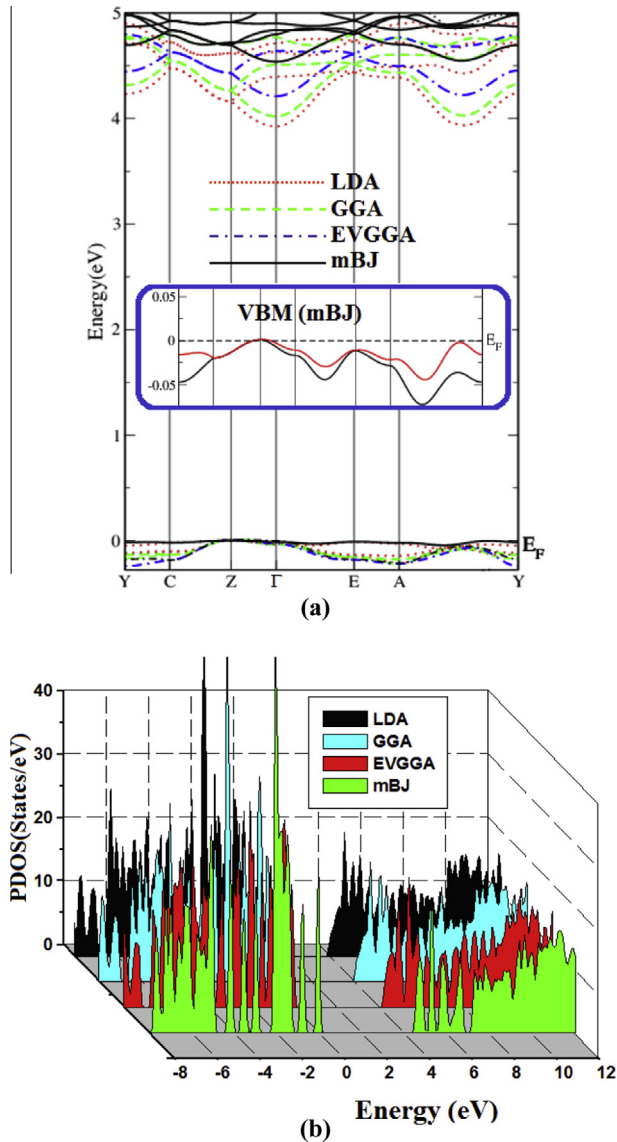
Fig. 2. (a) Calculated band structure; (b) total density of state of [Ag(D-his)]$_n$ semiconductor using LDA-(CP), GGA-PBE, EVGGA and mBJ.

Table 1
Calculated values of energy band gap E_g (eV) $\varepsilon_1^{average}(0)$, $\varepsilon_1^{xx}(0)$, $\varepsilon_1^{yy}(0)$ and $\varepsilon_1^{zz}(0)$ and $n^{xx}(0)$, $n^{yy}(0)$ and $n^{zz}(0)$ using LDA-(CP), GGA-PBE, EVGGA and mBJ.

	LDA	GGA	EVGGA	mBJ
E_g (eV)	3.92	4.02	4.22	4.54
$\varepsilon_1^{average}(0)$	1.63	1.93	1.48	1.31
$\varepsilon_1^{xx}(0)$	1.70	2.06	1.55	1.36
$\varepsilon_1^{yy}(0)$	1.45	1.65	1.31	1.18
$\varepsilon_1^{zz}(0)$	1.71	2.08	1.56	1.40
$n^{xx}(0)$	1.30	1.43	1.24	1.16
$n^{yy}(0)$	1.20	1.28	1.14	1.08
$n^{zz}(0)$	1.31	1.44	1.25	1.18

and O-2s state is small. The C-2s and N-2s state show strong hybridization in this energy range.

3.2. Electronic charge density

The charge density of [Ag(D-his)]$_n$ is derived from the reliable converge wave function which is used to study the bond nature

of the solids. The mBJ scheme was used for the calculation of total valence charge density that visualizes the charge transfer and bonding properties. The blue region in the ring represents maximum charge concentration as clear from thermo-scale which is due to strong covalent bond among N and C atoms and delocalize electron on the ring as shown in Fig. 4a. The O atom of the other monomers shares with hydrogen bond and form heterodimer. There are two hetrodimers per unit cell as shown in Fig. 4b. The calculated bond length of H and O is 1.67 Å. Fig. 4c shows strong covalent bond between N and C, while the contours forms between N and Ag shows strong covalent and partially ionic bond. The calculated analytical values in Table 2 also show bonding nature and percentage of ionicity in term of electronegativity difference {C(2.49), N(3.04), O(3.44) and Ag(1.93)} using Pauling selection rules [37]. The analytical results show close agreement to the valence charge density analysis.

3.3. Linear optical susceptibilities

Optical properties of solids can give deep insight into the electronic structure. It is not possible to improve photonic devices for optical communication purpose without proper understanding of optical properties of the used materials [38]. The present work mainly deals with dielectric function which is the most important aspect for the calculation of optical properties. We need to have the correct energy eigenvalues and electron wave functions for calculating the frequency dependent dielectric function $\varepsilon(\omega)$. Both energy eigenvalues and electron wave function are natural output of the calculating band structure. The symmetry of the [Ag(D-his)]$_n$ crystal structure allows five non-zero second order dielectric tensor components. For simplicity we select only three diagonal principal components $\varepsilon^{xx}(\omega)$, $\varepsilon^{yy}(\omega)$ and $\varepsilon^{zz}(\omega)$ along a, b and c crystallographic axis. The three components of the imaginary part of dielectric function completely define the linear optical properties. These components can be obtained using the expression taken from the Ref. [39].

$$\varepsilon_2^{ij} = \frac{4\pi^2 e^2}{Vm^2\omega^2} \times \sum_{nn'\sigma} \langle kn\sigma|p_i|kn'\sigma\rangle \langle kn'\sigma|p_j|kn\sigma\rangle$$
$$\times f_{kn}(1-f_{kn'})\delta(E_{kn'}-E_{kn}-\hbar\omega) \qquad (1)$$

where m and e represent mass and charge of electron and ω stand for the electromagnetic radiation striking the crystal, V correspond to volume of the unit cell, in bracket notation p represent the momentum operator, $|kn\sigma\rangle$ represent the crystal wave function with crystal momentum k and σ spin which correspond to the eigenvalue E_{kn}. The Fermi distribution function is represent by f_{kn} makes sure the counting of transition from occupied to unoccupied state and $\delta(E_{kn'}-E_{kn}-\hbar\omega)$ is the condition for conservation of total energy.

The inter-band transitions of the dielectric function $\varepsilon(\omega)$ can be split into direct and indirect transitions. We neglect the indirect inter-band transitions involving scattering of phonons that are expected to give a small contribution to $\varepsilon(\omega)$ [40].

The average value of three tensor components for real and imaginary parts of dielectric function were calculated as shown in Fig. 5a and b. Broadening is taken to be 0.1 eV which is typical of the experimental accuracy. The imaginary part of dielectric function $\varepsilon_2^{average}(\omega)$ obtained by mBJ shows better optical gap as compared to the CA-LDA, PBE-GGA and EV-GGA therefore it is selected for further explanation of linear and nonlinear optical susceptibilities. The peaks in the $\varepsilon_2(\omega)$ spectra are determined by the electric-dipole transitions between the occupied states to the unoccupied states as shown in Fig. 5c. The material show high transparency in the energy range between 0.0 and 4.54 eV. At around 4.54 eV the frequency of the incident photon become
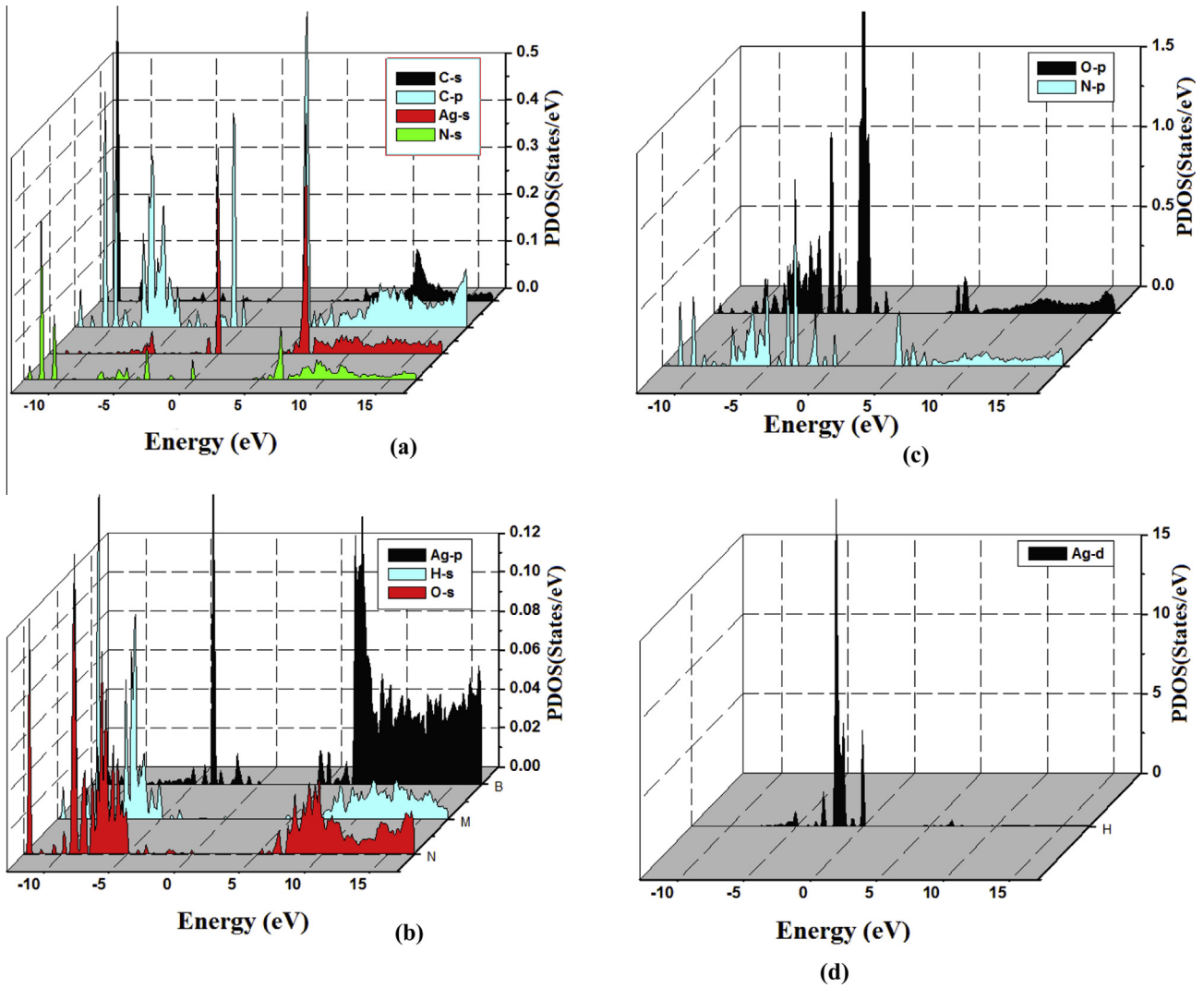
Fig. 3. Calculated partial densities of states (States/eV unit cell).

comparable to the frequency of dipole oscillation in crystal and absorption of photons occur at threshold frequency. The first critical point for $\varepsilon_2^{xx}(\omega)$, $\varepsilon_2^{yy}(\omega)$ and $\varepsilon_2^{zz}(\omega)$ occurs at 4.54 eV and first transition of electron occurs between valence and conduction band extreme. The first peak of $\varepsilon_2^{xx}(\omega)$, $\varepsilon_2^{yy}(\omega)$ and $\varepsilon_2^{zz}(\omega)$ components which is situated between 4.54 and 5.0 eV, is corresponding to the transition from valence band maximum to the conduction band minimum. Fig. 5c, also disclose considerable anisotropy among three polarization spectra except the range (9.5–10 and 13.2–13.5) eV where both $\varepsilon_2^{xx}(\omega)$ and $\varepsilon_2^{yy}(\omega)$ show isotropy. The main peaks of $\varepsilon_2^{xx}(\omega)$, $\varepsilon_2^{yy}(\omega)$ and $\varepsilon_2^{zz}(\omega)$ are located at 7.7, 13.2 and 6.3 eV respectively. It is clear that mBJ causes to shift all structures towards higher energy with lower amplitude as compared to LDA, GGA, EV-GGA [41]. The real part of optical dielectric function is related to the electric polarizability. It shows the optical response of the material to the electromagnetic radiation. The real part of the optical dielectric function can be calculated from Kramers–Kronig inversion using the imaginary part of dielectric function [42].

$$\varepsilon_1(\omega) = 1 + \frac{2}{\pi}P\int_0^{\infty}\frac{\omega'\varepsilon_2(\omega')}{\omega'^2 - \omega^2}d\omega' \qquad (2)$$

where P stand for principal value of integral. The calculated real part of the frequency dependent dielectric function $\varepsilon_1(\omega)$ is shown

in Fig. 5d. There is considerable anisotropy among $\varepsilon_1^{xx}(\omega)$, $\varepsilon_1^{yy}(\omega)$ and $\varepsilon_1^{zz}(\omega)$ except at 4.3, 5.2 and 7.7 eV where both of $\varepsilon_1^{xx}(\omega)$ and $\varepsilon_1^{zz}(\omega)$ components show isotropy, and the tail show isotropy among the three spectral components. The uniaxial anisotropy was calculated to be 0.0985, using the expression $\delta\varepsilon = \lfloor(\varepsilon_0^{ll} - \varepsilon_0^{\perp})/\varepsilon_0^{tot}\rfloor$ given in Ref. [43], which indicates a strong anisotropy among the three principal dielectric tensor components of $[Ag(D\text{-}his)]_n$.

The calculated imaginary and real parts of the frequency dependent dielectric function were used to calculate the refractive index $n(\omega)$, birefringence $\Delta n(\omega)$, absorption coefficient $I(\omega)$ and reflectivity $R(\omega)$. These are illustrated in Fig. 5e–h. The calculated static refractive index for three non-zero tensor components directly related to the $\varepsilon_1(0)$ through the relation $n(0) = \sqrt{\varepsilon_1(0)}$. In Table 1 we have listed the values of $n(0)$. With increasing the energy of the EM waves the three components of the refractive index increases to reach maximum value. There is sharp decrease in the highest peaks of $n^{xx}(\omega)$, $n^{yy}(\omega)$ and $n^{zz}(\omega)$ at 5.4, 7.3 and 5.9 eV. One can see that $n^{zz}(\omega)$ component exhibit sharp decrease and crosses the unity at 6.1 eV which show high luminescent nature of the material. One can also see the superluminality of the material from $\varepsilon_2(\omega)$. The sharp increase in $\varepsilon_2^{zz}(\omega)$ around 6.1 eV verifies the luminosity of material. The birefringence $\Delta n(\omega)$, is the difference between the refractive indices of the two linearly polarized beams known as extraordinary (n_e) and ordinary (n_0)
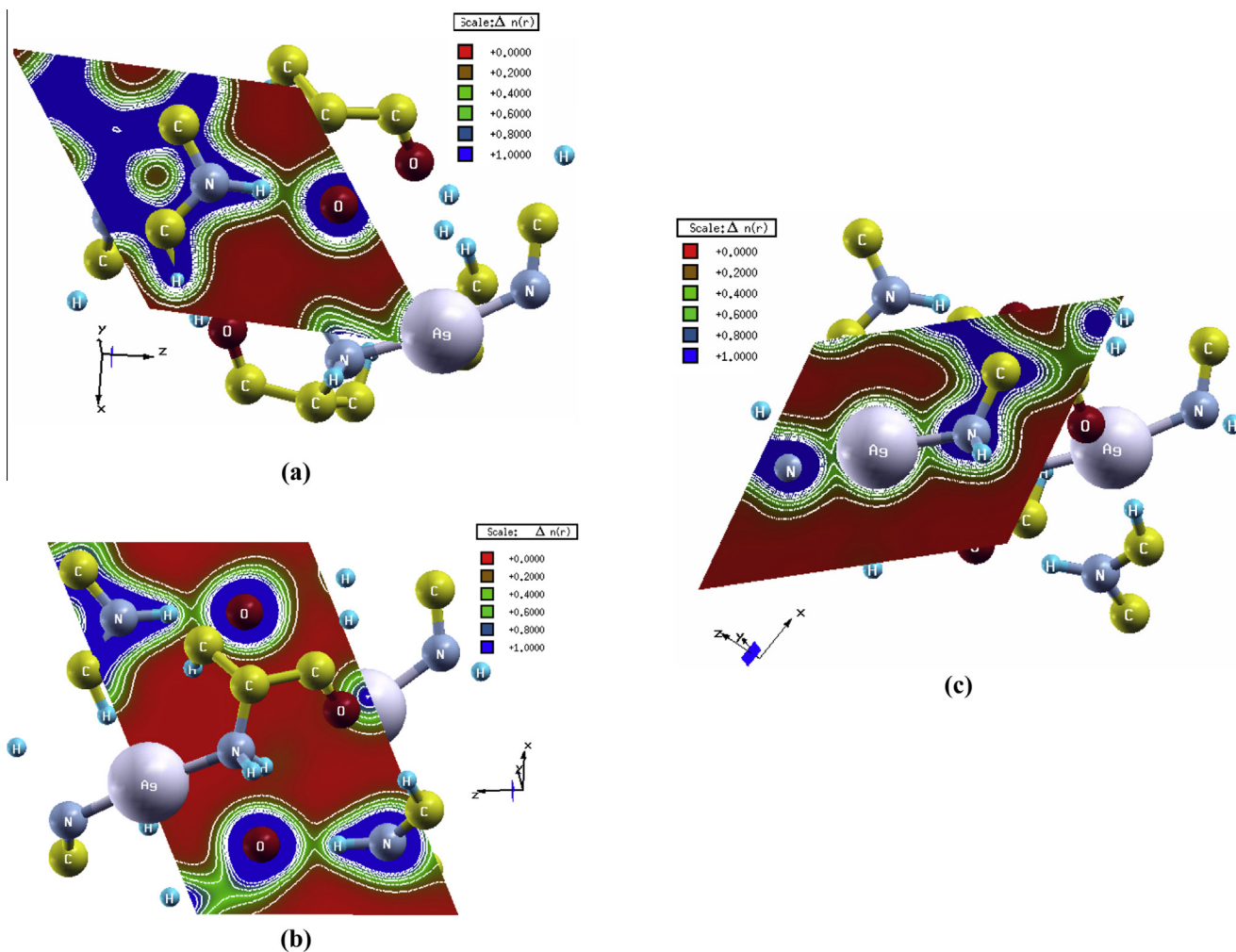
Fig. 4. Electronic charge density contour plots [Ag(D-his)]$_n$.

Table 2
The bonding nature and percentage of ionicity in term of electronegativity difference {C(2.49), N(3.04), O(3.44) and Ag(1.93)} using Pauling selection rules [37].

Bond	X_A–X_B	Polarity	%Ionicity
C2–N1	0.49	Non polar	8.88
C5–C4	0.00	Non polar	0.00
N3–Ag1	1.11	Polar	22.7
C8–O1	0.95	Polar	16.4

refraction indices i.e. $\Delta n = n_e - n_0$. Fig. 5f shows the birefringence $\Delta n(\omega)$ for [Ag(D-his)]$_n$. The birefringence is very significant in the non-absorbing region below the gap [44]. The curves show strong oscillations around zero which could be broadened out by selecting a larger broadening. The calculated value of birefringence at zero energy is 0.06.

The frequency dependent absorption coefficient elucidates high transparency of the compound in energy range between 0.0 and 4.5 eV. The $I^{xx}(\omega)$ is foremost in the energy range 4.5–5.8 eV and 7.0–9.0 eV while $I^{zz}(\omega)$ component is more responsible for absorption of light in energy range 5.8 to 7.0 eV and from 9.2 to 12.5 eV. The contribution of $I^{yy}(\omega)$ at lower energy range is small, then it

reach the maximum value between 12.4 and 13.5 eV showing isotropy with $I^{xx}(\omega)$.

The spectral components of reflectivity spectra show high transparency and negligible reflection in infrared and visible region. The dominant peaks of $R^{xx}(\omega)$ and $R^{zz}(\omega)$ are located at 7.8 and 6.2 eV resulting in a 6.0% and 13.5% reflection whereas $R^{yy}(\omega)$ show negligible contribution for the whole range except the high energy. From investigation of reflectivity spectra one can see that [Ag(D-his)]$_n$ is suitable for antireflection coating materials for the solar cells.

3.4. Nonlinear optical susceptibilities

The nonlinear organic crystals are very important because it can generate high second and third harmonic generation and hyperpolarizabilities which offer a building block role for new generation photonic devices [45]. The complex second-order nonlinear optical susceptibility tensor $\chi^{(2)}_{ijk}(-2\omega; \omega; \omega)$ are generally written as [46–49]:

$$\chi^{ijk}_{inter}(-2\omega; \omega, \omega) = \frac{e^3}{\hbar^2} \sum_{nml} \int \frac{d\vec{k}}{4\pi^3} \frac{\vec{r}^i_{nm}\{\vec{r}^j_{ml}\vec{r}^k_{ln}\}}{(\omega_{ln} - \omega_{ml})}$$
$$\times \left\{ \frac{2f_{nm}}{(\omega_{mn} - 2\omega)} + \frac{f_{ml}}{(\omega_{ml} - \omega)} + \frac{f_{ln}}{(\omega_{ln} - \omega)} \right\} \quad (3)$$
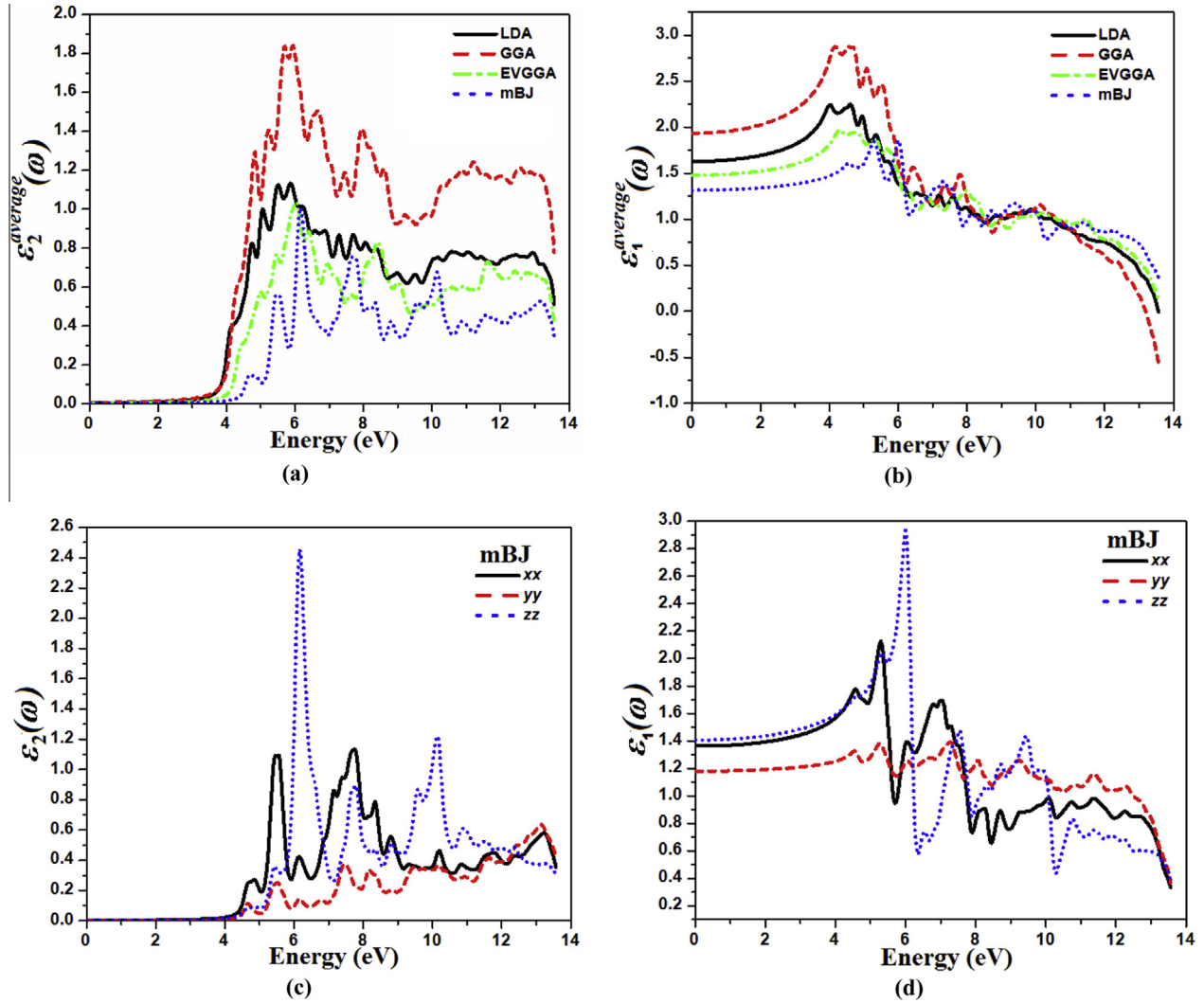
Fig. 5. (a) Calculated $\varepsilon_2^{average}(\omega)$; (b) calculated $\varepsilon_1^{average}(\omega)$; (c) calculated $\varepsilon_2^{xx}(\omega)$, $\varepsilon_2^{yy}(\omega)$ and $\varepsilon_2^{zz}(\omega)$; (d) calculated $\varepsilon_1^{xx}(\omega)$, $\varepsilon_1^{yy}(\omega)$ and $\varepsilon_1^{zz}(\omega)$; (e) calculated $n^{xx}(\omega)$, $n^{yy}(\omega)$ and $n^{zz}(\omega)$; (f) calculated birefringence (Δn); (g) calculated $I^{xx}(\omega)$, $I^{yy}(\omega)$ and $I^{zz}(\omega)$; (h) calculated $R^{xx}(\omega)$, $R^{yy}(\omega)$ and $R^{zz}(\omega)$.

In the given expressions one can see the three main contributions to $\chi_{ijk}^{(2)}(-2\omega;\omega;\omega)$: the intra-band transitions $\chi_{intra}^{ijk}(-2\omega;\omega,\omega)$: inter-band transitions $\chi_{inter}^{ijk}(-2\omega;\omega,\omega)$ and the modulation of inter-band terms by intra-band terms $\chi_{mod}^{ijk}(-2\omega;\omega,\omega)$, for $n \neq m \neq l$. Where n represent the valence states, m the conduction states and l stands for all states ($l \neq m, n$). Two types of transitions are occur, the first one is vcc' in which one valence band (v) and two conduction bands (c and c') are involved, the second transition is represented by $vv'c$ where v and v' show two valence bands and one conduction band denoted by c. Where $\Delta_{nm}^i(\vec{k}) = \vartheta_{nn}^i(\vec{k}) - \vartheta_{mm}^i(\vec{k})$ with $\vec{\vartheta}_{nm}^i$ being the i component of the electron velocity given as $\vartheta_{nm}^i(\vec{k}) = i\omega_{nm}(\vec{k})r_{nm}^i(\vec{k})$ and $\left\{ r_{nm}^i(\vec{k})r_{ml}^j(\vec{k}) \right\} = \frac{1}{2}(r_{nm}^i(\vec{k})r_{ml}^j(\vec{k}) + r_{nm}^j(\vec{k})r_{ml}^i(\vec{k}))$. Using the expression $r_{nm}^i(\vec{k}) = \frac{P_{nm}^i(\vec{k})}{im\omega_{nm}(\vec{k})}$, [50] one can calculate $r_{nm}^i(\vec{k})$ by using the position matrix elements element P_{nm}^i between the band states n and m having energy difference of $\hbar\omega_{nm} = \hbar(\omega_n - \omega_m)$. f_{nm} represent the Fermi distribution function where $f_{nm} = f_n - f_m$. Aspnes [51] exposed that only the one-electron virtual transitions which occur between one valence band state and two conduction band states (vcc') contribute significantly to the second-order tensor. The virtual-hole contribution is ignored ($vv'c$) because it was found to be negative and smaller than the virtual-electron contribution.

For simplicity we symbolize $\chi_{ijk}^{(2)}(-2\omega;\omega;\omega)$ as $\chi_{ijk}^{(2)}(\omega)$ where subscripts i, j, and k represent Cartesian indices.

Since the crystal structure of the meso silver(I) histidinate [Ag(D-his)]$_n$ is monoclinic, thus it allows eight non-zero complex second-order nonlinear optical susceptibility tensors namely, 112, 123, 211, 222, 213, 233, 312 and 323. Fig. 6a represents the calculated $|\chi_{ijk}^{(2)}(\omega)|$ for eight tensor components which show that $|\chi_{213}^{(2)}(\omega)|$ has the highest value at static limit 1.57 pm/V and 2.34 pm/V at $\lambda = 1064$ nm, as compared to the other components therefore it is the dominate component. Thus, the static values are very important for the estimation of second harmonic generation (SHG) efficiency [52].

Further, the real and imaginary part of complex second-order nonlinear optical susceptibility tensors for the dominant component $\chi_{213}^{(2)}$ are shown in Fig. 6b.

To analyze the features of the calculated eight non-zero complex second-order nonlinear optical susceptibility tensors spectra, it would be worthwhile to compare the absolute value of the dominant component $|\chi_{213}^{(2)}(\omega)|$ with the imaginary part of the dielectric function $\varepsilon_2(\omega)$ as a function of both $\omega/2$ and ω as illustrated in Fig. 6c. The spectral structure in the energy range between 2.27 and 5.54 eV is originated from 2ω resonance while the next structure from 4.54 to 6.80 eV is formed by the combination of ω and 2ω struc-

$$\chi^{ijk}_{intra}(-2\omega;\omega,\omega) = \frac{e^3}{\hbar^2}\int\frac{d\vec{k}}{4\pi^3}\left[\sum_{nml}\omega_{nm}\vec{r}^i_{nm}\left\{\vec{r}^j_{ml}\vec{r}^k_{ln}\right\}\left\{\frac{f_{nl}}{\omega^2_{ln}(\omega_{ln}-\omega)}-\frac{f_{lm}}{\omega^2_{ml}(\omega_{ml}-\omega)}\right\}-8i\sum_{nm}\frac{f_{nm}\vec{r}^i_{nm}\left\{\Delta^j_{mn}\vec{r}^k_{nm}\right\}}{\omega^2_{mn}(\omega_{mn}-2\omega)}\right.$$
$$\left.+2\sum_{nml}\frac{f_{nm}\vec{r}^i_{nm}\left\{\vec{r}^j_{ml}\vec{r}^k_{ln}\right\}(\omega_{ml}-\omega_{ln})}{\omega^2_{mn}(\omega_{mn}-2\omega)}\right] \tag{4}$$

$$\chi^{ijk}_{mod}(-2\omega;\omega,\omega) = \frac{e^3}{2\hbar^2}\int\frac{d\vec{k}}{4\pi^3}\left[\sum_{nml}\frac{f_{nm}}{\omega^2_{mn}(\omega_{mn}-\omega)}\left\{\omega_{nl}\vec{r}^i_{lm}\left\{\vec{r}^j_{mn}\vec{r}^k_{nl}\right\}-\omega_{lm}\vec{r}^i_{nl}\left\{\vec{r}^j_{lm}\vec{r}^k_{mn}\right\}\right\}-i\sum_{nm}\frac{f_{nm}\vec{r}^i_{nm}\left\{\vec{r}^j_{mn}\Delta^k_{mn}\right\}}{\omega^2_{mn}(\omega_{mn}-\omega)}\right] \tag{5}$$
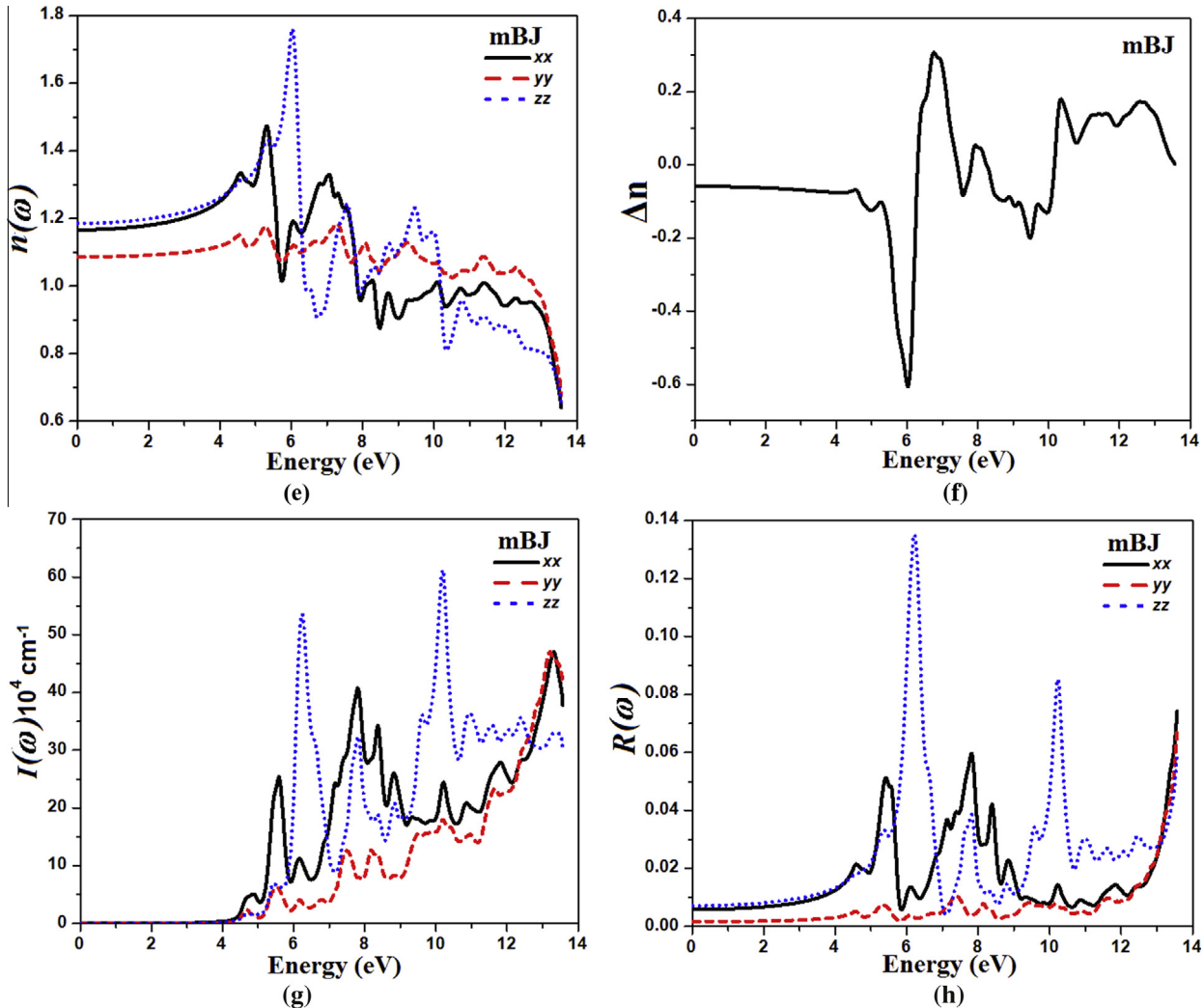

Fig. 5 (continued)

tures. The third structure form 4.54 to 6.80 eV is originated from ω resonance. We have calculated the microscopic first hyperpolarizability β_{ijk} vector component along the principal dipole moment directions for $\chi^{(2)}_{213}(\omega)$ component at static limit and at $\lambda = 1064$ nm using the expression given in Ref. [53]. The calculated value of $\beta^{(2)}_{213}(\omega)$ are 0.965×10^{-30} esu and 0.666×10^{-30} esu, respectively.

4. Conclusion

The complete characterization of meso silver(I) histidinate [Ag(D-his)]$_n$ has not been fully described in the previous literature due to its complex chemical behaviors. In the present work the electronic band structure, density of states, total valence charge density and optical properties of [Ag(D-his)]$_n$ were calculated using density functional theory (DFT) based on full potential linear augmented plane wave (FPLAPW) method. The exchange correlation effect was treated using Ceperley–Alder (CA) local density approximation (CA-LDA), Perdew–Burke–Ernzerhof generalized gradient approximation (PBE-GGA), Engel Voskov generalized gradient approximation (EV-GGA) and recently developed modified Becke and Johnson (mBJ) approximation. The calculated band structure shows that the compound is a semiconductor having
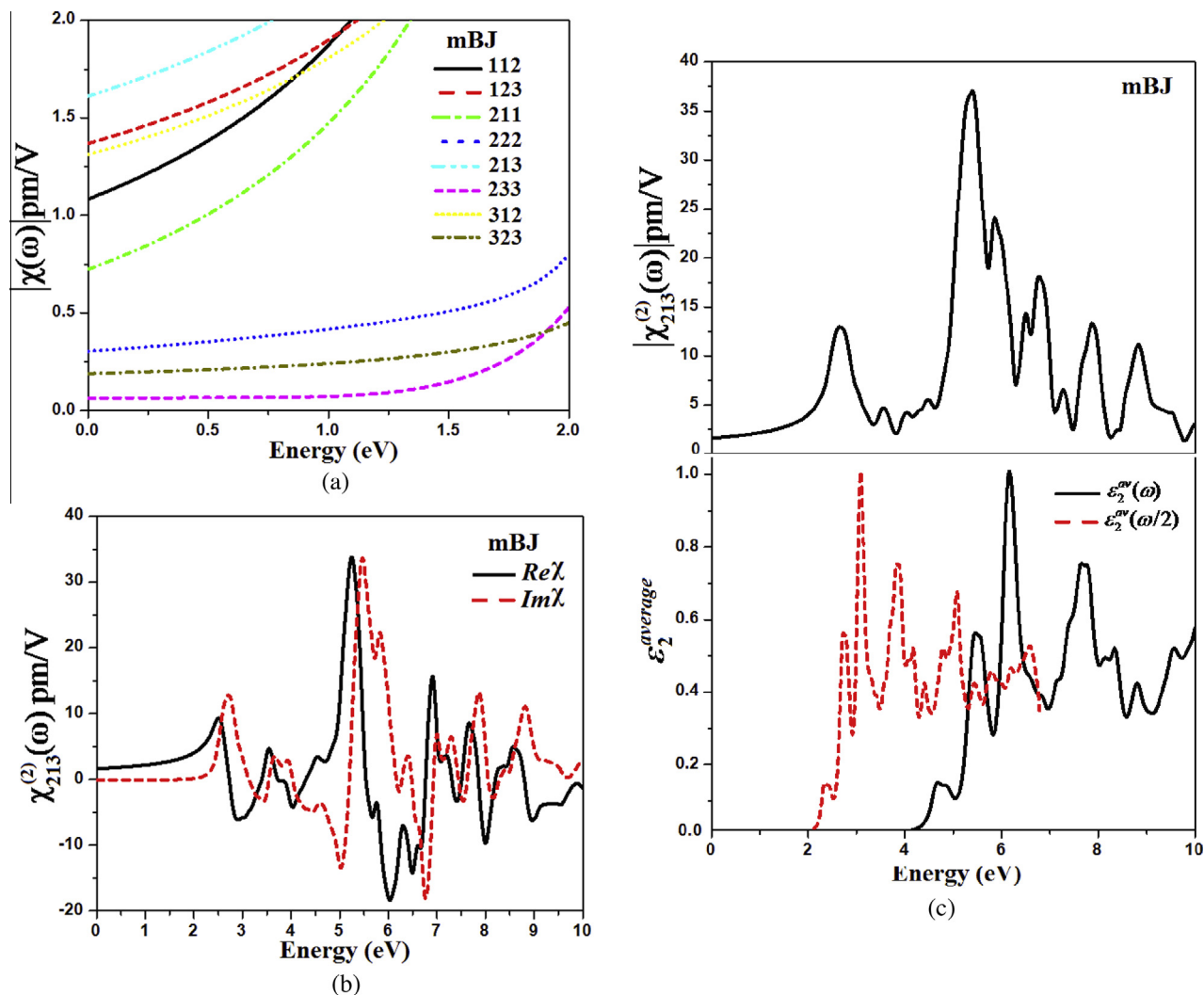
Fig. 6. (a) Calculated $|\chi_{ijk}^{(2)}(\omega)|$ for eight components using mBJ; (b) calculated real and imaginary of $\chi_{213}^{(2)}(\omega)$; (c) calculated $|\chi_{213}^{(2)}(\omega)|$ and $\varepsilon_2^{average}(\omega)$ along with $\varepsilon_2^{average}(\omega/2)$.

indirect ($Z \rightarrow \Gamma$) band gap of 3.92 eV (LDA), 4.02 eV (GGA), 4.21 eV (EVGGA), and 4.54 eV (mBJ). We should emphasize that mBJ give good results due to better band splitting, thus mBJ was selected for presenting the results. The effective mass ratio for electron, light and heavy holes were calculated in conduction band minimum, upper valence band maximum and lower valence band maximum. Strong hybridization between orbitals confirm the covalent nature of the bonds and provide the details about bands formation in $[Ag(D\text{-}his)]_n$. The total valence charge density contour plots shows the strong covalent nature with small contribution of ionicity in $[Ag(D\text{-}his)]_n$ bonds. The charge density contour plot visualized two heterodimers between O and H bond in a unit cell. The calculated length of the bond between O and H, of the heterodimer, is 1.67 Å. The average value of real and imaginary part of dielectric function was calculated. The three principal tensor components of $\varepsilon_2(\omega)$, $\varepsilon_1(\omega)$, $n(\omega)$, $I(\omega)$ and $R(\omega)$ were calculated and discussed in detail. The calculated uniaxial anisotropic value (0.0985) and briefings (0.06) indicates the strong anisotropy of the optical dielectric function of $[Ag(D\text{-}his)]_n$. The investigation $n(\omega)$ spectra shows the superluminality in ultraviolet region while $R(\omega)$ spectra shows that $[Ag(D\text{-}his)]_n$ is suitable for antireflection coating material for solar cells in infrared and visible region. The second harmonic generation was calculated and analyzed. Meso silver(I) histidinate acquire SHG of 1.64 pm/V at static limit and 2.34 pm/V at λ = 1064 nm. We also have calculated the microscopic first hyper-

polarizability $\beta_{213}^{(2)}(\omega)$ at static limit to be 0.965×10^{-30} esu and at λ = 1064 nm of about 0.666×10^{-30} esu.

Acknowledgments

References

[1] Saeed Ahmad, Anvarhusein A. Isab, Saqib Ali, Abdul Rahman Al-Arfaj, Polyhedron 25 (2006) 1633.
[2] R.H. Holm, E.I. Solomon (Eds.), Bioinorganic enzymology, Chem. Rev. 96 (7) (1996).
[3] Z. Guo, P.J. Sadler, Angew. Chem., Int. Ed. 38 (1999) 1512.
[4] P.J. Blower, Annu. Rep. Prog. Chem., Sect. A 96 (2000) 645.
[5] C.X. Zhang, S.J. Lippard, Curr. Opin. Chem. Biol. 7 (2003) 481.
[6] R.A. Sanchez-Delgado, A. Anzellotti, Mini Rev. Med. Chem. 4 (2004) 23.
[7] M.C. Gimeno, A. Laguna, Comprehensive Coordination Chemistry II, vol. 6, Elsevier, Oxford, 2004. p. 911.
[8] C.F. Shaw III, Chem. Rev. 99 (1999) 2589.
[9] C.B. Acland, H.C. Freeman, Chem. Commun. 1016 (1971).
[10] K. Nomiya, H. Yokoyama, J. Chem. Soc., Dalton Trans. 2483 (2002).
[11] P.A. Demaret, F. Abraham, Acta Crystallogr., Sect. C 43 (1987) 1519.
[12] K. Nomiya, S. Takahashi, R. Noguchi, S. Nemoto, T. Takayama, M. Oda, Inorg. Chem. 39 (2000) 3301.

[13] M.E. Kamwaya, E. Papavinasam, S.G. Teoh, R.K. Rajaram, Acta Crystallogr., Sect. C 40 (1984) 318.
[14] M.E. Kamwaya, E. Papavinasam, S.G. Teoh, R.K. Rajaram, Z. Kristallogr. 169 (1984) 51.
[15] K. Nomiya, I. Azumaya, N.C. Kasuga, T. Kato, Curr. Top. Biochem. Res. 10 (2008) 1.
[16] K. Nomiya, K. Tsuda, N.C. Kasuga, J. Chem. Soc., Dalton Trans. 1653 (1998).
[17] K. Nomiya, K. Tsuda, T. Sudoh, M. Oda, J. Inorg. Biochem. 68 (1997) 39.
[18] Noriko Chikaraishi Kasuga, Yoshitaka Takagi, Shin-ichiro Tsuruta, Wataru Kuwana, Rie Yoshikawa, Kenji Nomiya, Inorg. Chim. Acta 368 (2011) 44.
[19] S. Gao, Comput. Phys. Commun. 153 (2003) 190.
[20] K. Schwarz, J. Solid State Chem. 176 (2003) 319.
[21] S.A. Khan, A.H. Reshak, Z.A. Alahmed, J. Mater. Sci. 49 (2014) 5208.
[22] K.M. Wong, S.M. Alay-e-Abbas, A. Shaukat, Y. Fang, Y. Lei, J. Appl. Phys. 113 (2013) 014304.
[23] K.M. Wong, S.M. Alay-e-Abbas, Y. Fang, A. Shaukat, Y. Lei, J. Appl. Phys. 114 (2013) 034901.
[24] Available at: <http://www.ccdc.cam.ac.uk>.
[25] P. Balaha, K. Shewartz, G.K.H. Madsen, D. Kvsnicka, J. Luitz, WIEN2K, An Augmented Plane Wave +Local Orbitals Program for Calculating Crystals Properties, Karlheinz Schewartz, Techn. Universitat, Wien, Austria, 2001, ISBN 3-9501031-1-2.
[26] D.M. Ceperley, B.I. Alder, Phys. Rev. Lett. 45 (1980) 566.
[27] J.P. Perdew, K. Burke, M. Ernzerhof, Phys. Rev. Lett. 77 (1996) 3865.
[28] E. Engel, S.H. Voskov, Phys. Rev. B 47 (1993) 13164.
[29] F. Tran, P. Blaha, Phys. Rev. Lett. 102 (2009) 226401.
[30] A.H. Reshak, S. Azam, Appl. Phys. A 116 (2014) 333.
[31] A.H. Reshak, S.A. Khan, Mater. Res. Bull. 48 (2013) 4555.
[32] A.H. Reshak, W. Khan, J. Alloys Compd. 592 (2014) 92.
[33] A.H. Reshak, S.A. Khan, S. Auluck, RSC Adv. 4 (2014) 11967.
[34] M. Benkraouda, N. Amrane, J. Alloys Compd. 546 (2013) 151.
[35] San.-Dong Guo, Bang.-Gui Liu, J. Magn. Magn. Mater. 324 (2012) 2410.
[36] H. Hakan Gürel, Özden Akinci, Hilmi Ünlü, Superlattices Microstruct. 51 (2012) 725.
[37] Schlusseltechnologien Key Technologies, 41st IFF Springschool, 2010, pp A1–18.
[38] S.A. Khan, A.H. Reshak, Int. J. Electrochem. Sci. 8 (2013) 9459.
[39] A. Delin, P. Ravindran, O. Eriksson, J.M. Wills, Int. J. Quant. Chem. 69 (1998) 349.
[40] N.V. Smith, Phys. Rev. B 3 (1971) 1862.
[41] A.H. Reshak, H. Kamarudin, S. Auluk, J. Phys. Chem. B 116 (2012) 4677.
[42] H. Tributsch, Naturforsch. A 32A (1977) 972.
[43] A.H. Reshak, Xuean Chen, S. Auluck, I.V. Kityk, J. Chem. Phys. 129 (2008) 204111.
[44] A.H. Reshak, S. Auluck, I.V. Kityk, Phys. Rev. B 75 (2007) 245120.
[45] Mario Rodriguez, Gabriel Ramos-Ortiz, Jose Luis Maldonado, Victor M. Herrera-Ambriz, Oscar Dominguez, Rosa Santillan, Norberto Farfan, Keitaro Nakatani, Spectrochim. Acta, Part A 79 (2011) 1757.
[46] S. Sharma, J.K. Dewhurst, C. Ambrosch-Draxl, Phys. Rev. B 67 (2003) 165332.
[47] A.H. Reshak, (Ph.D. thesis), Indian Institute of Technology-Rookee, India, 2005.
[48] A.H. Reshak, J. Chem. Phys. 125 (2006) 014708.
[49] A.H. Reshak, J. Chem. Phys. 124 (2006) 014707.
[50] C. Ambrosch-Draxl, J. Sofo, Comput. Phys. Commun. 175 (2006) 1.
[51] D.E. Aspnes, Phys. Rev. B 6 (1972) 4648.
[52] A.H. Reshak, H. Kamarudin, S. Auluck, J. Mater. Sci. 48 (2013) 1955.
[53] R.Y. Boyed, Principles of non linear optics. Academic Press is an imprint of Elsevier. ISBN: 978-0-12-369470-6.